A Comprehensive Model for Non-Aqueous Lithium Air Batteries Involving Different Reaction Mechanisms

Kan-Hao Xue,[a,b,*] Euan McTurk,[c] Lee Johnson,[c] Peter G. Bruce,[c,d,*] and Alejandro A. Franco[a,b,e,*,z]

[a]*Laboratoire de Réactivité et Chimie des Solides, UMR CNRS 7314, Université de Picardie Jules Verne, 80039 Amiens Cedex, France*
[b]*Réseau sur le Stockage Electrochimique de l'Energie (RS2E), FR CNRS 3459, France*
[c]*Department of Materials, University of Oxford, Oxford OX1 3PH, United Kingdom*
[d]*Department of Chemistry, University of Oxford, Oxford OX1 3QR, United Kingdom*
[e]*ALISTORE-ERI, European Research Institute, FR CNRS 3104, F-80039 Amiens Cedex 1, France*

There are various reaction mechanisms in the discharge process of a non-aqueous lithium air battery (LAB). Recently, it has been identified that low current rate and high donor number solvents can lead to solution phase reaction, but high current rate and low donor number solvents will cause thin film growth covering the active cathode surface. In this paper we extend our previous LAB multiscale model, which considers the thin film growth mode, to the general case where both surface thin film growth and solution phase reaction coexist. A detailed mechanism is proposed and simulation results are compared with experimental data.
 [DOI: 10.1149/2.0121504jes] All rights reserved.

Manuscript submitted October 6, 2014; revised manuscript received December 26, 2014. Published January 22, 2015.

The non-aqueous lithium air battery[1,2] (referred to here as LAB) possesses a supreme theoretical energy density[3–5] and consequently has attracted much attention. Although significant progress has been made toward identifying and mitigating the limitations in LABs,[6–12] very little is still known about the mechanisms and processes behind the discharge dynamics, which are not only important for the realization of LABs for practical use, but also have considerable impact on how results from current LABs are interpreted.

A number of continuum mathematical models have been proposed to characterize the discharge behavior of LABs,[11,13–20] and most models are based on solving transport equations for O_2 and Li^+,[13–20] together with Butler-Volmer[14,19] or Tafel[13,15–17] electrode kinetics. However, recently it has been identified that the morphology of the discharge product, mainly Li_2O_2, may depend on the solvent[21,22] as well as on the current rate.[23,24] In the so-called surface-limited reaction case,[25,26] a Li_2O_2 thin film covers the active surface (see route A in Fig. 1), while in the so-called solution phase reaction case[27,28] the intermediate species O_2^- tends to diffuse to some preferential nucleation sites through the electrolyte, followed by disproportionation and nucleation/growth (see route B in Fig. 1). The resulting Li_2O_2 morphologies are discs, toroids or small particles.[29] Here we assume that the first reduction reaction is the same in both cases:

$$O_{2(sol)} + e^- \xrightarrow{\text{surface}} O^-_{2(sol)} \qquad [1]$$

where the subscript "sol" stands for solution phase, though a more complicated procedure involving Li^+ may occur:

$$O_{2(sol)} + Li^{+*} + e^- \xrightarrow{\text{surface}} LiO^*_2$$

where the star sign indicates adsorbed species. However, the second reduction reaction may take place at different locations. In the surface-limited reaction case, two possible reactions may occur:

$$O_2^{-*} + 2Li^{+*} + e^- \xrightarrow{\text{surface}} Li_2O_{2(film)} \qquad [2]$$

$$2O_2^{-*} + 2Li^{+*} \longrightarrow Li_2O_{2(film)} + O_2 \uparrow \qquad [3]$$

where O_2^{-*} stems from the locally adsorbed O_2^- in Eq. 1. However, the generated oxygen molecule in Eq. 3 can then be easily reduced to form O_2^- due to its proximity to the active surface. Hence, the overall reaction of 1 and 3 is equivalent to that of 1 and 2. On the other hand, in the solution phase reaction case, the second-stage reaction is on the nucleation sites:

$$2O^-_{2(sol)} + 2Li^+{}_{(sol)} \longrightarrow Li_2O_{2(particle)} + O_2 \uparrow \qquad [4]$$

thus the overall reactions are 1 and 4. The discrepancy in the reaction mechanisms forces us to treat the two cases in different mathematical ways.

Some recent modelling attempts try to consider both mechanisms, such as the rate-dependent Li_2O_2 growth model of Horstmann et al.,[30] and the kinetic model of oxygen reduction from Safari et al.,[31] which neglects the possibility of electron tunneling through thin Li_2O_2 films. Nevertheless, to our knowledge no whole-cell level model taking into account both reaction mechanisms simultaneously has been reported before. Typical whole-cell models developed recently are considering thin film growth[32] or island growth[33] modes, both falling into the surface limited mechanism category. In our previous works[11,34] we proposed a discharge model of LAB within a multiscale framework,[11,35] by considering the detailed microstructural properties of the cathode and the surface limited reaction mechanism only. Here we present an extension of it to include the solution phase reaction mechanism. We still consider a Super P carbon black as the prototype cathode, but our modelling framework may apply to other types of active materials,

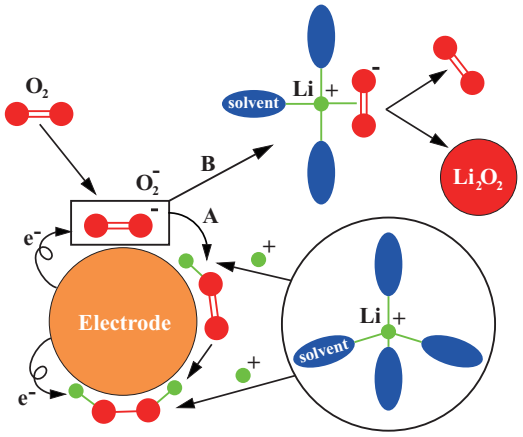

Figure 1. Illustration of the two mechanisms for oxygen reduction in aprotic solvents. In route A, the second reduction occurs at the electrode surface, while in route B, O_2^- is slightly bonded to the lithium ion, which may wander to an existing solid Li_2O_2 core which promotes a disproportionation reaction.

*Electrochemical Society Active Member.
zE-mail: alejandro.franco@u-picardie.fr

including Au,[4] TiC,[36] etc., as well as other cathode topologies (e.g. carbon fibers).

Model Development

Reaction mechanism.— The cathode microstructure and in particular the pore size distribution (PSD) are known to substantially impact the performance of LABs.[11,37,38] We consider a composite cathode with an experimentally measured PSD in nanometer to micrometer range representative of the Super P carbon. The associated surface area distribution to this PSD is shown in Fig. 3. Here we term "the hall" the largest open space across the porous structure of the cathode filled with electrolyte, which corresponds to the big pores with size larger than the measured range in Fig. 3. While the size of the hall is very large, its specific area is small compared with all the small pores. In our model, the hall is treated as a container where Li_2O_2 particle nucleation and growth can take place. This is inspired from the experimental observation of Li_2O_2 particles with several hundred nanometers size.[23,39,40]

As the hall surface area is much lower than the pore surface area, it follows that the first oxygen reduction reaction (Eq. 1) mainly occurs in the smaller pores, in which O_2^- radicals are initially generated. If we assume Li^+ and LiO_2 are involved in the first reduction, an alternative treatment is required and this is given in the Appendix. However, here we focus on the simple reaction scheme 1.

The further reduction of O_2^- into O_2^{2-} follows two possible paths and these are (i) consecutive reduction in the pores; and (ii) disproportionation on the surface of an existing Li_2O_2 particle. Selection of either route is determined primarily by the mobility of $O_2{}^-$ between pores. Consequently, we define an escape function $\chi(r)$, where r is the pore radius, which characterizes the percentage of O_2^- in the $Li^+ - O_2^- - n$ solvent solvated complex form[28] to escape the pore of radius r toward the hall where most of the nucleation and growth is assumed to occur. Hence, the two second reduction reaction pathways can be written as:

$$O^-_{2(sol)} \longrightarrow \chi(r)O^-_{2(sol)} + [1-\chi(r)]\,O_2^{-*}$$

$$\text{Route A}: [1-\chi(r)]\,O_2^{-*} + 2\,[1-\chi(r)]\,Li^{+*} + [1-\chi(r)]\,e^- \xrightarrow{\text{surface}} [1-\chi(r)]\,Li_2O_{2(film)} \quad [5]$$

$$\text{RouteB}: \chi(r)O^-_{2(sol)} + \chi(r)Li^+{}_{(sol)} \longrightarrow \left[\frac{\chi(r)}{2}\right] Li_2O_{2(particle)} + \left[\frac{\chi(r)}{2}\right] O_2 \uparrow \quad [6]$$

which together with reaction 1 give

$$O_2 + 2Li^+ + 2e^- \longrightarrow \left[\frac{\chi(r)}{2-\chi(r)}\right] Li_2O_{2(particle)} + 2\left[\frac{1-\chi(r)}{2-\chi(r)}\right] Li_2O_{2(film)} \quad [7]$$

We explicitly discriminate Li_2O_2 particles from Li_2O_2 thin films because only the latter will cause surface passivation and block electron transport, which is a key factor when determining the discharge capacity in our model. It follows that the mathematical form of the escape function is the key to discriminate solution phase reaction from surface-limited reaction. To determine such a mathematical form, a pore network model is used as schematized in Fig. 4. Note that $O_2{}^-$ radicals in smaller pores find it harder to enter the hall, because they usually have to go across a longer path than radicals in larger pores. In the simplest model, we may consider a number of pore classes: the hall being the largest, then the 1st class pores, the 2nd class pores until the N^{th} class pores which are the smallest pores in the porous cathode network. This structural scheme obviously neglects other inter-class interconnections, but more sophisticated networks can be adopted without major difficulty. Through the open mathematical form of the escape function, the methodology behind this simple model accepts results from more detailed pore network analysis.

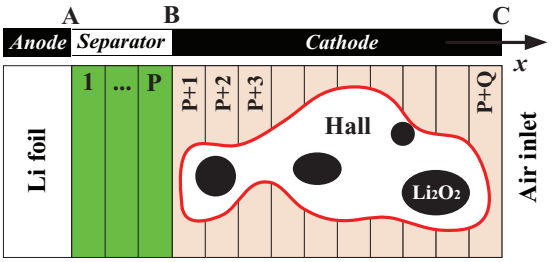

Figure 2. Schematic illustration of the lithium air battery under consideration, and of the implemented finite difference bins.

Now we assume ξ to be the escape probability for a $O_2{}^-$ radical from an i^{th} class pore to the $(i\text{-}1)^{th}$ class pore adjacent to it. In principle ξ can be a function of i, but for simplicity we assume ξ to be a constant. Then the total escape function for an N^{th} class pore is

$$\chi\,[r\,(N)] = \xi^N \quad [8]$$

where the pore radius r is determined by the class index N. Accepting the assumption that a suitable escape function can be an exponential one, we may write in a continuous form:

$$\chi\,(r) = \xi^{\frac{r_{max}-r}{r_{max}}} \quad [9]$$

where the value of ξ ($0 \le \xi \le 1$) is assumed to be mainly dependent on the donor number of the solvent used. As the life time of $O_2{}^-$ in the high donor number solvents is longer, ξ will be a number close to 1. Therefore, in this case, $O_2{}^-$ possesses a high probability of diffusing to the hall and nucleating into particles there. In addition, the ξ value is also highly sensitive to current rate because a high current tends to pile up intermediate species near the surface, promoting thin film formation. In other words, ξ value will be smaller at higher current rates for the same solvent.

Oxygen transport.— Having set up the reaction mechanisms, we follow our previous approach to model the species transport. As in Ref. [34], we neglect the transport of Li^+ since its concentration is much higher than oxygen. The main transport equation considered is for oxygen diffusion

$$\frac{\partial}{\partial t}\left[(1-s)\,\varepsilon_0 c\right] = \frac{\partial}{\partial x}\left[(1-s)^{1.5}\varepsilon_0^{1.5} D_0 \left(\frac{\partial c}{\partial x}\right)\right] - \frac{a\,j_{Far}}{\nu F} \quad [10]$$

where c is the averaged O_2 concentration in each bin (*cf.* Fig. 2); ε_0 is the initial porosity; D_0 is the intrinsic oxygen diffusion coefficient in the electrolyte; a is the specific surface area; j_{Far} is the faradaic current density; $\nu = 2$ is the number of electrons involved in the overall reaction 7; F is the Faraday constant and s is defined to be a "saturation"[34] which is a measure of choked pore volume compared with initial total pore volume, and can be defined in either of the following ways:

$$s \equiv \frac{V_{Li_2O_2}}{\varepsilon_0 V} \quad [11]$$

or

$$\varepsilon = (1-s)\varepsilon_0 \quad [12]$$

where $V_{Li_2O_2}$ is the real-time discharge product volume inside a chosen volume element V, and ε is the real-time porosity in that local region. Obviously, s evolves over time and should be calculated by the model. The term $(1-s)^{1.5}\varepsilon_0^{1.5}$ thus represents a Bruggeman-like correction to the diffusion coefficient in porous structures. Note that while some oxygen can be released in the second reduction reaction 6, the overall reaction can be written as 7, where only an oxygen sink term (relevant to faradaic current) appears but no source term needs to be considered in Eq. 10.

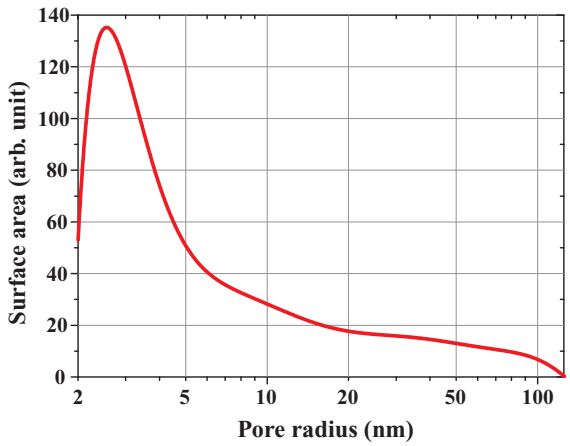

Figure 3. Surface area distribution in the prototype Super P carbon LAB cathode considered in this work, derived from the experimentally measured PSD.

Electrode kinetics.— The faradaic reduction current density is assumed to be given by a Butler-Volmer equation

$$j_{\text{Far}} = \nu F k c \left\{ \exp\left(-\frac{\beta F \eta}{RT}\right) - \exp\left[\frac{(1-\beta) F \eta}{RT}\right] \right\} \quad [13]$$

where k is the kinetic rate, β is the charge transfer coefficient and η is the Butler-Volmer overpotential. We assume the rate-limiting step is the first one-electron process, as reflected by the form inside the exponential term. j_{Far} is multiplied by $\nu = 2$ to account for the two-step reduction. In addition, j_{Far} is proportional to the oxygen concentration c rather than $c^{1-\beta}$, as confirmed by experiments.[41] It has to be noted here that, more generally, electrochemical double layer effects should impact this faradaic current (e.g. transport of charged species at the vicinity of the active material, confinement of the ions in the pores, and polarization effects due to the solvent). These can be modelled following the approach recently proposed by us,[42] which is out of the scope of this paper but its implications will be studied in the future.

The remaining unsolved variables in Eq. 10 are s and a, which will be addressed in the following sections.

Saturation.— To estimate the saturation term we select a particular bin #i and monitor the discharge product precipitation from the beginning of a fresh discharge (see Fig. 5). The total amount of substance for Li_2O_2 in this bin at time t is given by integrating the faradaic current over time:

$$n^{[i]}(t) = \frac{1}{\nu F} \int_0^t a^{[i]}(t') V j_{\text{Far}}^{[i]}(t') dt' \quad [14]$$

where V is the volume of our selected volume element (naturally being the volume of a cathode bin) and the superscript $[i]$ indicates that the quantity is calculated in bin #i.

By means of the density of Li_2O_2, we can transform the amount of substance into the volume of Li_2O_2:

$$V_{\text{Li}_2\text{O}_2}^{[i]}(t) = \left(\frac{M_{\text{Li}_2\text{O}_2}}{\rho_{\text{Li}_2\text{O}_2}}\right) n^{[i]}(t) = \frac{M_{\text{Li}_2\text{O}_2}}{\nu F \rho_{\text{Li}_2\text{O}_2}} \int_0^t a^{[i]}(t') V j_{\text{Far}}^{[i]}(t') dt' \quad [15]$$

which together with Eq. 11 leads to

$$s^{[i]}(t) = \frac{M_{\text{Li}_2\text{O}_2}}{\varepsilon_0 \nu F \rho_{\text{Li}_2\text{O}_2}} \int_0^t a^{[i]}(t') j_{\text{Far}}^{[i]}(t') dt' \quad [16]$$

In Eq. 16, the active surface area $a^{[i]}$ is still unknown – only the initial values at $t = 0$ are given.

Active surface area.— For simplicity we have divided the pores into two categories by size: detailed PSD is considered below 125 nm,

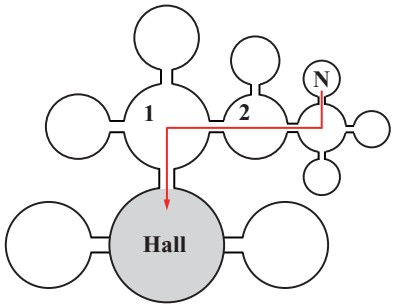

Figure 4. The pore network model considered in this work for evaluating the mathematical form of the escape function.

while any pore with its radius greater than 125 nm is regarded as the hall. The active surface area of the hall is neglected, while we discretize the 0–125 nm pore radius range into N meshes. For a selected volume element V (shown in Fig. 5) in bin #i, the total initial active surface area (when no discharge product exists, or $t = 0$) of a particular mesh j (located at pore radius $r_{[j]}$) can be evaluated as

$$A_{[j]}^{[i]}(0) = a_0 V \left[\frac{\alpha_0(r_{[j]})}{\sum_{j'} \alpha_0(r_{[j']})} \right] \quad [17]$$

where a_0 is the intrinsic specific surface area for the cathode material, thus $a_0 V$ is the total active surface area, while the fraction within the square bracket characterizes the percentage of active surface area falling into mesh j. Here $\alpha_0(r)$ is the surface area distribution function for the cathode material, where a typical example is shown in Fig. 3.

We write $[j]$ or $[j']$ in the subscript in order to emphasize that they represent a particular mesh in the pore radius range, while the superscript $[i]$ is used exclusively to specify the particular cathode bin index. Due to our meshing scheme, the parameter $r_{[j]}$ is simply calculated by

$$r_{[j]} \equiv \frac{125\, j}{N} \quad [18]$$

with a unit of nanometer.

When $t > 0$, $A_{[j]}^{[i]}(t)$ in volume element V suffers from two degradation mechanisms. The first one has a geometric origin, since a thin film covering a pore will lead to a smaller pore radius than the initial value. By assuming spherical pores, this relation is straightforward and is obtained as

$$\alpha_0(r) \to \left(\frac{r-\delta}{r}\right)^2 \alpha_0(r)$$

where δ is the thickness of the film covering the pore surface, in the unit of nanometer. The other performance degradation mechanism is due to electron transport limitation, because Li_2O_2 is known to be an insulator with a bandgap estimated to be 4.81–6.37 eV.[43–45]

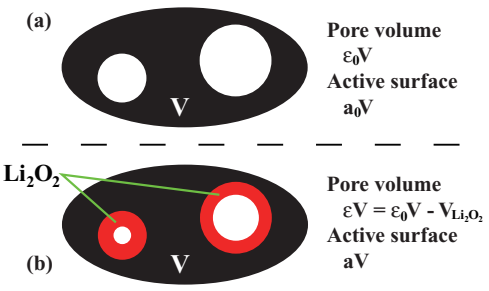

Figure 5. Demonstration of the pore volume and active surface area for (a) a porous cathode structure without discharge products; (b) the same structure with a certain amount of Li_2O_2 deposited in the pores.

The actual electron conductivity through Li_2O_2 thin films during the discharge process is attributed to tunnelling effect,[25] hole conduction[46] or in particular polaron hopping.[47] Here we accept the conclusion of Viswanathan et al.[25] that the maximum electron tunnelling distance is through 5–10 nm Li_2O_2 thin film, and implement the same tunnelling probability function as in our previous work.[34] To sum up, the real active surface area distribution function is

$$\alpha(r) = \left(\frac{r-\delta}{r}\right)^2 \left[\frac{1-\mathrm{erf}(\delta-7)}{2}\right] \alpha_0(r) \quad [19]$$

which implies that the real-time total active surface area in the selected volume element V should be

$$A^{[i]}_{[j]}(t) = a_0 V \left[\frac{r_{[j]} - \delta^{[i]}_{[j]}(t)}{r_{[j]}}\right]^2 \left\{\frac{1-erf\left[\delta^{[i]}_{[j]}(t)-7\right]}{2}\right\} \times \left\{\frac{\alpha_0(r_{[j]})}{\sum_{j'} \alpha_0(r_{[j']})}\right\} \quad [20]$$

Hence, the real-time specific surface area in bin #i, $a^{[i]}(t)$, can be obtained by first letting the volume V be that of a cathode bin, and then summing up $A^{[i]}_{[j]}(t)$ over all pore radius meshes:

$$a^{[i]}(t) = \sum_j a^{[i]}_{[j]}(t) \quad [21]$$

where

$$a^{[i]}_{[j]}(t) = \frac{A^{[i]}_{[j]}(t)}{V} = a_0 \left[\frac{r_{[j]} - \delta^{[i]}_{[j]}(t)}{r_{[j]}}\right]^2 \left\{\frac{1-erf\left[\delta^{[i]}_{[j]}(t)-7\right]}{2}\right\} \times \left\{\frac{\alpha_0(r_{[j]})}{\sum_{j'} \alpha_0(r_{[j']})}\right\} \quad [22]$$

In Eq. 22, the only unknown parameter is the film thickness $\delta^{[i]}_{[j]}(t)$, which is obtained following the approach presented in the next section.

Film thickness.— In our model we take an approximation that the oxygen concentration in each bin is homogeneous throughout the pores, therefore the faradaic current density is uniformly distributed over all active surface for each particular bin #i, according to the Butler-Volmer equation 13. Nevertheless, the film thickness is non-uniform in each bin, but should depend on the pore radius. The reason is that the percentage of Li_2O_2 forming a thin film, compared with the total Li_2O_2, is related to the pore radius through the escape function. For each pore radius mesh, we shall monitor the film thickness, $\delta^{[i]}_{[j]}(t)$, in real-time.

Mathematically, we first write the total amount of Li_2O_2, no matter whether deposited in the hall as particles or precipitated locally as a thin film, stemming from the pore radius mesh #j in bin #i, as

$$n^{[i]}_{[j]}(t) = \frac{1}{\nu F}\int_0^t a^{[i]}_{[j]}(t')V j^{[i]}_{\mathrm{Far}}(t')dt' \quad [23]$$

Yet, the real amount of Li_2O_2 forming a thin film is modified when taking into account the escape function:

$$n^{[i]}_{\mathrm{film},[j]}(t) = \frac{1}{\nu F}\int_0^t a^{[i]}_{[j]}(t')V \left[\frac{2-2\chi\left(r_{[j]}\right)}{2-\chi\left(r_{[j]}\right)}\right] j^{[i]}_{\mathrm{Far}}(t')dt' \quad [24]$$

therefore

$$\frac{d\delta^{[i]}_{[j]}(t)}{dt} = 10^9 \times \left(\frac{M_{Li_2O_2}}{\rho_{Li_2O_2} a^{[i]}_{[j]}(t) V}\right) \frac{dn^{[i]}_{\mathrm{film},[j]}(t)}{dt} = 10^9 \times \left(\frac{2M_{Li_2O_2}}{\nu F \rho_{Li_2O_2}}\right)\left[\frac{1-\chi(r_{[j]})}{2-\chi(r_{[j]})}\right] j^{[i]}_{\mathrm{Far}}(t) \quad [25]$$

where the 10^9 factor transforms the unit from meter to nanometer. Equation 25 together with an initial condition for film thickness gives the real-time film thickness for each pore radius mesh, in each bin.

Cell potential.— The Butler-Volmer overpotential is treated approximately as homogeneous in our model due to the following reason. The practical current rate in a LAB is usually very low such that the electrolyte phase potential varies only slightly across the cathode, while the solid phase potential is homogeneous because of the high conductivity in the cathode particles. When η is homogeneous, by summing up the faradaic currents in all the bins we can inversely obtain η through the overall discharge current density J, based on Eq. 13. By assuming that $\beta = 0.5$ for the sake of simplicity, the cell voltage is calculated by

$$U = U_0 - \frac{2RT}{F}\sinh^{-1}\left(\frac{J}{\sum_i 2\nu a_i \Delta x F k c}\right) - JR_s - JR_{\mathrm{film}} \quad [26]$$

where U_0 is the equilibrium cell voltage, R_s is the series resistance which includes the contribution from the electrolyte resistance and the anode overpotential, and the JR_{film} term represents the contribution from the Li_2O_2 film resistance. In order to evaluate JR_{film} we notice that near the end of discharge (when the voltage drop across the Li_2O_2 film is prominent) more discharge current is carried by the part of cathode closest to the air inlet. As an approximate treatment, we assume

$$R_{\mathrm{film}} = \frac{\varrho\,\delta}{a_0 \Delta x} \quad [27]$$

where δ is the film thickness in bin #P+Q for the largest-size pore considered, here as the pores with 125 nm radius. Both the series resistance R_s and the Li_2O_2 resistivity ϱ will be fixed by fitting to the experimental discharge curves.

The equilibrium cell voltage U_0 has long been regarded as 2.959 V by theoretical calculation,[48,49] but recent experimental investigations give a more reasonable value of 2.861 V at 25°C.[50] In our model we shall take

$$U_0 = 2.861\mathrm{V} \quad [28]$$

Experimental

The LAB cell under investigation consisted of a Li_xFePO_4 anode, an 840 μm thick porous separator (92.1% porosity) and a *c.a.* 100 μm thick carbon black composite cathode (81.9% porosity).

The Li_xFePO_4 anode was prepared by mixing $LiFePO_4$ powder (MTI Corporation), "Super P Li" carbon (TIMCAL) and PTFE (Aldrich) in a gravimetric ratio of 8/0.5/1, adjusting the formula for the dilution of the PTFE in aqueous suspension. Each anode contained 30 mg active material. The anodes were rinsed in 1/1 ethanol/distilled water for 30 minutes, then chemically precharged in a bath of 250 mL distilled water, 3.6 mL hydrogen peroxide (Fisher) and 1.5 mL acetic acid (Sigma Aldrich) for 30 minutes. The anodes were then rinsed in distilled water and vacuum dried at 140°C in a Buchi oven overnight.

The Super P Li cathodes were prepared by mixing Super P Li with PTFE in a gravimetric ratio of 9/1 and spreading onto 180 grade stainless steel mesh (Advent Research Materials Ltd), which acts as a substrate and current collector. Each cathode contained 1.5 mg active material. The cathodes were then rinsed in 1/1 ethanol/distilled water for 30 minutes and vacuum dried at 140°C in a Buchi oven overnight.

The components were assembled in Swagelok cells consisting of a Li_xFePO_4 anode, two Whatman glass microfiber separators wetted with electrolyte and a Super P Li cathode. The Swagelok cells were sealed in glass cases, which were then flushed with oxygen prior to cycling on a Biologic VMP3 potentiostat.

In our experiments, two solvents with different donor numbers were chosen: tetraethylene glycol dimethyl ether (TEGDME, donor number 16.6,[51] viscosity 3.294 mPa · s at 298.15 K[52]) and dimethyl

Table I. Experimental cell parameters.

	Symbol	Value	Unit
General parameters			
Cathode thickness[a]	L_{cat}	100	μm
Separator thickness[a]	L_{sep}	840	μm
Cell area[a]	$\mathcal{A}$	0.5	cm^2
Specific carbon surface area of the cathode[a]	a_0	1.98×10^7	m^{-1}
TEGDME cell parameters			
Saturated O_2 concentration[b]	c_{sat}	4.43	$mol \cdot m^{-3}$
O_2 diffusion coefficient in pure solvent[a]	D_0	2.4×10^{-9}	$m^2 \cdot s^{-1}$
Kinetic rate of O_2/O_2^- reduction[c]	k	1.11×10^{-7}	$m \cdot s^{-1}$
DMSO cell parameters			
Saturated O_2 concentration[b]	c_{sat}	1.86	$mol \cdot m^{-3}$
O_2 diffusion coefficient in pure solvent[a]	D_0	3.7×10^{-9}	$m^2 \cdot s^{-1}$
Kinetic rate of O_2/O_2^- reduction[c]	k	2.10×10^{-6}	$m \cdot s^{-1}$

[a]Measured.
[b]Calculated from the O_2 Bunsen coefficients measured in reference.[55]
[c]From reference.[28]

sulfoxide (DMSO, donor number 29.8,[53] viscosity 1.99 mPa · s at 298.15 K).[54] The salt is 0.5 M lithium trifluoromethanesulfonate (Li triflate). The Li_xFePO_4 anode was used in place of lithium foil to avoid reaction between Li and DMSO, while the cell voltage may be transformed into a hypothetical Li-anode cell by shifting the cell voltage upwards by 3.45 V, the equilibrium potential of $LiFePO_4/FePO_4$ with respect to Li/Li^+. Other parameters can be found in Table I.

Both cells were discharged galvanostatically at three current rates: 0.1 mA, 0.2 mA and 0.5 mA absolute currents, corresponding to 2 $A \cdot m^{-2}$, 4 $A \cdot m^{-2}$ and 10 $A \cdot m^{-2}$ apparent current densities, respectively.

Simulation

All simulations were carried out using LRCS home-made MATLAB codes. The model is developed as part of the multiscale modelling framework MS LIBER-T,[56] which is designed as a single simulation package with multiple applications for electrochemical cells and energy conversion devices.

For the finite difference simulation, the separator is divided equally into 84 bins while the cathode is divided equally into 10 bins. The cathode bins involve mesoscale calculations and are more computationally demanding. The convergence of our finite difference mesh is fulfilled through careful tests. The initial oxygen concentration in the electrolyte is assumed to be homogeneous across the cell separator and cathode, equalling to the saturated value.

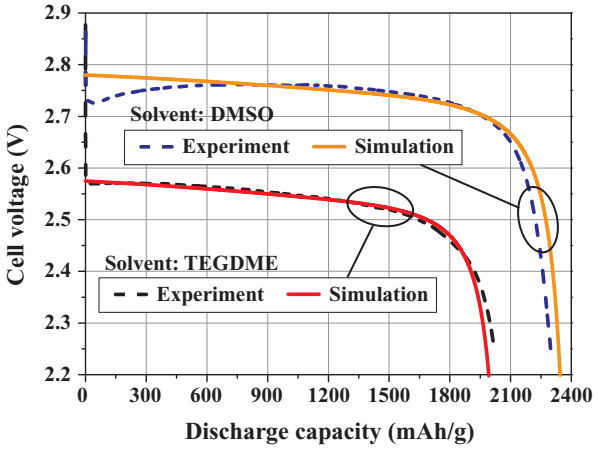

Figure 6. Discharge curve simulation for the TEGDME and DMSO cells with comparison to experiments. The discharge current density is 2 $A \cdot m^{-2}$.

Table II. Parameters in the 2 $A \cdot m^{-2}$ rate simulation determined by fitting to experimental curves.

	Fitted values	
Parameters	TEGDME	DMSO
Escape parameter ξ	0.48	0.55
Li_2O_2 thin film resistivity ϱ	3×10^{10} Ω · m	3×10^{10} Ω · m
Series resistance R_s	0.14 Ω · m^2	0.04 Ω · m^2

Low discharge rate.— At a current density of 2 $A \cdot m^{-2}$, the simulated discharge curves of TEGDME and DMSO cells are compared with experiments in Fig. 6. Some parameters are fitted to the experimental curves and are listed in Table II. It can be seen that the Li_2O_2 thin film resistivity can be chosen as the same in both TEGDME and DMSO cells at this discharge rate, but the series resistance in TEGDME cell is much larger than in DMSO cell, possibly due to the high electrolyte resistance and viscosity in TEGDME solution. In both cells, the simulated discharge curves fit well the experiments, while the ξ value is slightly larger in DMSO cell (0.55) compared with TEGDME cell (0.48), which is consistent with our intuitive guess because DMSO possesses a higher donor number.

Since the escape rates from pores with different sizes are generally different, the film thickness evolution rate is also non-uniform among the pore sizes even within the same bin. Figures 7a and 7b demonstrate such differences within the last bin, where the 5 nm and 60 nm pores experience fast thin film growth, while the 120 nm pore has a slow film growth rate. Due to the tunnelling function implemented in this

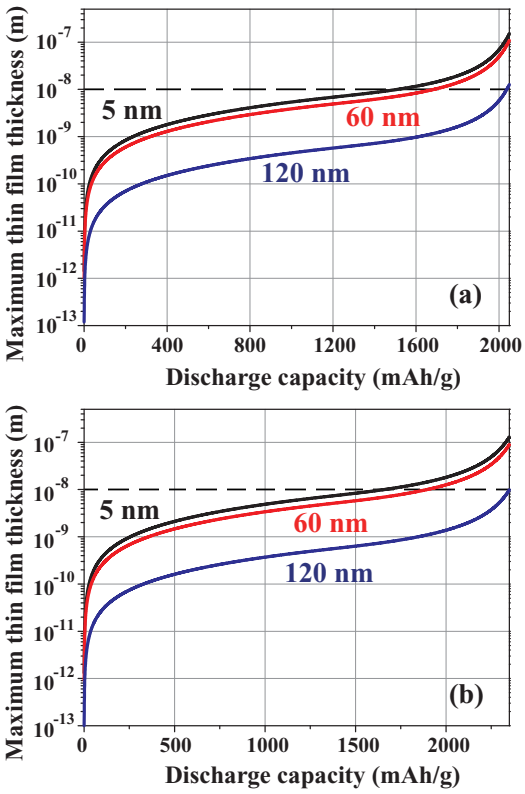

Figure 7. Evolution of the maximum film thickness in various pores within the last bin (bin #*P*+*Q*) of: (a) the TEGDME cell; (b) the DMSO cell. Three different pore ranges are demonstrated: 5 nm (black), 60 nm (red) and 120 nm (blue). The discharge current density is 2 $A \cdot m^{-2}$.

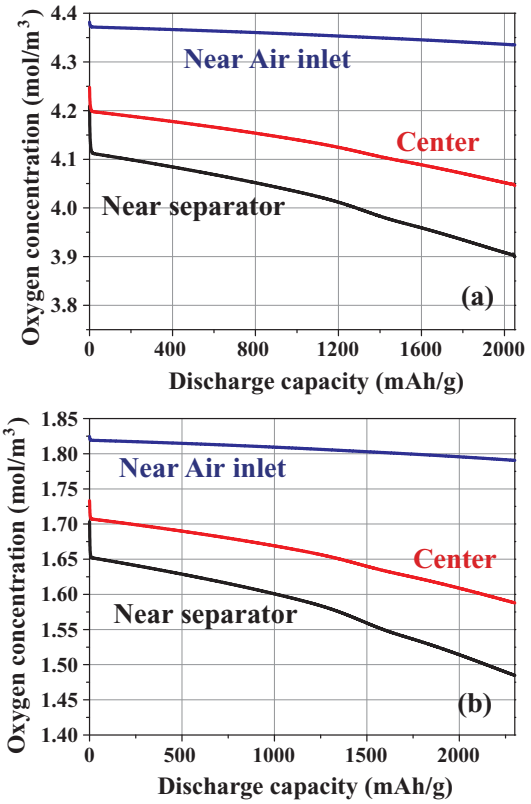

Figure 8. Evolution of the oxygen concentrations at three different locations of the cathode for: (a) the TEGDME cell; (b) the DMSO cell. The discharge current density is 2 $A \cdot m^{-2}$.

work, any pore with maximum film thickness beyond 10 nm (the horizontal dashed line) actually only has a very minor part still active. Therefore, for both TEGDME and DMSO cells we find that the end of discharge is signified by a total surface passivation of the largest pores (e.g. around 120 nm as in the figures). This indicates that the available surface area is the crucial factor for discharge capacity for the two cells in our study, which shows the same trend as the 100% thin film growth mode in our previous research,[34] and is consistent with a previous experimental discharge capacity–cathode surface area analysis over seven carbon black materials.[57]

The oxygen concentration profile is monitored during the simulation. Figure 8 shows that oxygen depletion does not occur in either of the cells throughout the discharge process. Rather, even in the deep cathode region closest to the separator one finds around 3.9 mol/m^3 and 1.5 mol/m^3 oxygen concentrations in the TEGDME and DMSO cells, respectively. Hence, the relatively short cathode design allows for sufficient usage of the whole cathode volume in our experiments.

Intermediate discharge rate.— At a current density of 4 $A \cdot m^{-2}$, the fitting parameters are shown in Table III while the simulation–experiment comparison is shown in Fig. 9. In both cells, the ξ values are slightly reduced compared with the 2 $A \cdot m^{-2}$ case, confirming

Table III. Parameters in the 4 $A \cdot m^{-2}$ rate simulation determined by fitting to experimental curves.

	Fitted values	
Parameters	TEGDME	DMSO
Escape parameter ξ	0.40	0.44
Li_2O_2 thin film resistivity ϱ	4×10^{10} $\Omega \cdot m$	2×10^{10} $\Omega \cdot m$
Series resistance R_s	0.09 $\Omega \cdot m^2$	0.04 $\Omega \cdot m^2$

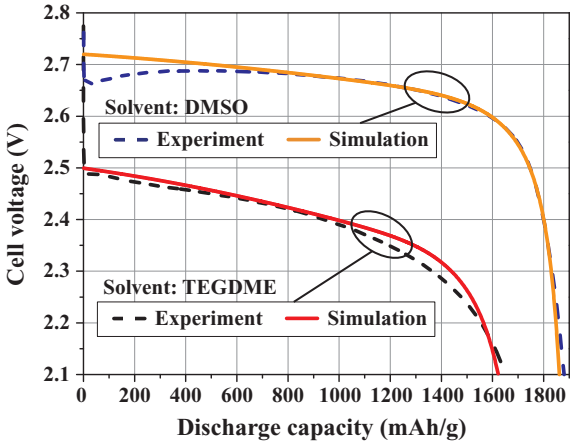

Figure 9. Discharge curve simulation for the TEGDME and DMSO cells with comparison to experiments. The discharge current density is 4 $A \cdot m^{-2}$.

that the escape function is dependent on the current rate. To gain more insights, we simulated the two cells again at 4 $A \cdot m^{-2}$, but using the same ξ values as in the low discharge rate case, i.e., 0.48 for the TEGDME cell and 0.55 for the DMSO cell. The resulting discharge capacities (not shown in the figures) are around 1900 mAh/g and 2300 mAh/g for the TEGDME and DMSO cells, respectively. These simulated values are in fact very close to the low discharge rate results. Hence, the escape function is indeed crucial for predicting the discharge capacities. Without a variation of ξ, the model only predicts almost the same discharge capacities at 2 $A \cdot m^{-2}$ and 4 $A \cdot m^{-2}$. A possible reason for this lies in that the cathode is very short in our experiments, thus the oxygen transport is not a limiting factor for discharge capacity, which is best demonstrated in Fig. 8.

High discharge rate.— At a current density of 10 $A \cdot m^{-2}$, the simulated discharge capacities of TEGDME and DMSO cells are both larger than experimental values even when ξ is set to zero, as shown in Fig. 10 (other fitted parameters are shown in Table IV). This confirms that both cells experience surface-limited reaction at this rate, consistent with the results by Adams et al.[24] who showed that thin film formation dominates the LAB reaction when a sufficiently high rate is reached. On the other hand, we believe that the discrepancy between simulation and experiment at high discharge rates may be attributed to lithium transport limitations. While the initial lithium ion concentration is much higher than that of oxygen, lithium ions in the cathode may be depleted at very high discharge rates because (i)

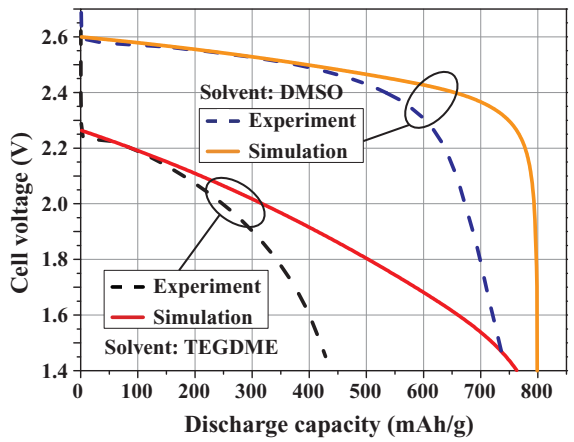

Figure 10. Discharge curve simulation for the TEGDME and DMSO cells with comparison to experiments. The discharge current density is 10 $A \cdot m^{-2}$.

Table IV. Parameters in the 10 A · m^{-2} rate simulation determined by fitting to experimental curves.

	Fitted values	
Parameters	TEGDME	DMSO
Escape parameter ξ	0	0
Li_2O_2 thin film resistivity ϱ	$2 \times 10^9\ \Omega \cdot m$	$5 \times 10^8\ \Omega \cdot m$
Series resistance R_s	$0.06\ \Omega \cdot m^2$	$0.03\ \Omega \cdot m^2$

their diffusion path, through the thick separator, is much longer than oxygen; (ii) their diffusion coefficient is also lower than oxygen.

Conclusions and Perspectives

We have set up a comprehensive model for non-aqueous lithium air batteries, accounting for both solution phase reaction and surface limited reaction. The extent to which the reaction is in solution phase mode is described through an escape function, which is a measure of the probability of O_2^- radicals to reach the largest open space of the cathode where they may disproportionate to form Li_2O_2 particles. Simulation of two cells with TEGDME and DMSO as solvents, respectively, confirms that the escape rate is higher in a high donor number solvent such as DMSO. The simulated discharge curves fit the experimental curves fairly well under low and intermediate discharge rates. In prospect, we envisage a more sophisticated pore network modelling approach to be compared with the current simple escape function form proposed in this work. In addition, the mismatch at very high discharge rates deserves further investigation.

We underline that the approach presented in this paper may be of some interest for the modelling of other battery technologies, such as lithium sulfur batteries.

Acknowledgments

Prof. Dominique Larcher and Dr. Trong-Khoa Nguyen at LRCS are gratefully acknowledged for helpful discussions. The support of Prof. Jean-Marie Tarascon (Collège de France, Paris) and Dr. Mathieu Morcrette at LRCS is greatly appreciated. Prof. Franco deeply acknowledges the Conseil Régional de Picardie and the European Regional Development Fund for the funding support through the project MASTERS.

Appendix: An Alternative Reaction Scheme

The first reduction reaction could be considered to involve Li^+

$$O_{2(sol)} + Li^{+*} + e^- \xrightarrow{\text{surface}} LiO_2^* \qquad [A1]$$

followed by the further dissolution of $LiO_2{}^*$

$$LiO_2^* \rightleftarrows O_{2(sol)}^- + Li^+{}_{(sol)} \qquad [A2]$$

the extent of which depends on the solubility of LiO_2 in that particular solvent. This is a key factor for judging the reaction mode, since only dissolved O_2^- may contribute to the solution phase reaction. Therefore, we re-write Eq. A2 by explicitly introducing a ratio factor λ as

$$LiO_2^* \longrightarrow (1-\lambda)\,LiO_2^* + \lambda\,O_{2(sol)}^- + \lambda\,Li^+{}_{(sol)} \qquad [A3]$$

Subsequently, the second reduction process occurs for the surface-limited part as

$$(1-\lambda)\,LiO_2^* + (1-\lambda)\,Li^{+*} + (1-\lambda)\,e^- \xrightarrow{\text{surface}} (1-\lambda)\,Li_2O_{2(film)} \qquad [A4]$$

and

$$\lambda(1-\chi)\,O_2^{-*} + \lambda(1-\chi)\,Li^{+*} \longrightarrow \left[\frac{\lambda(1-\chi)}{2}\right] Li_2O_{2(film)} + \left[\frac{\lambda(1-\chi)}{2}\right] O_2 \uparrow \qquad [A5]$$

where we introduce the same ratio factor χ as in the main text, which characterizes the percentage of O_2^- generated in Eq. A3 that are not involved in the further surface reduction. In other words, Eq. A5 implies as a priori that the solution phase O_2^- is partially adsorbed on the local electrode surface

$$O_{2(sol)}^- \longrightarrow \chi\,O_{2(sol)}^- + (1-\chi)\,O_2^{-*} \qquad [A6]$$

Obviously, the rest of the solution phase O_2^- not consumed by Eq. A5 will be subject to a disproportionation reaction at the preferred nucleation sites, which is exactly the so-called solution phase reaction. Hence, the second reduction in the solution phase mode is written explicitly as

$$\lambda\chi\,O_{2(sol)}^- + \lambda\chi\,Li^+{}_{(sol)} \longrightarrow \left(\frac{\lambda\chi}{2}\right) Li_2O_{2(particle)} + \left(\frac{\lambda\chi}{2}\right) O_2 \uparrow \qquad [A7]$$

Finally, in general we can summarize Eqs. A1, A3, A4, A5, and A7 into a global reaction

$$O_2 + 2Li^+ + 2e^- \longrightarrow \left(\frac{\lambda\chi}{2-\lambda}\right) Li_2O_{2(particle)} + \left[\frac{2-\lambda-\lambda\chi}{2-\lambda}\right] Li_2O_{2(film)} \qquad [A8]$$

which, though with one more escape function, can be compared with Eq. 7.

List of Symbols

Symbol	Parameter name	Unit
a	Specific surface area	m^{-1}
a_0	Initial specific surface area	m^{-1}
A	Total active surface area of a bin	m^2
$\mathcal{A}$	Superficial area	m^2
c	O_2 molar concentration	$mol \cdot m^{-3}$
c_{sat}	Saturated O_2 molar concentration	$mol \cdot m^{-3}$
D_0	O_2 diffusion coefficient	$m^2 \cdot s^{-1}$
F	Faraday constant	$C \cdot mol^{-1}$
I	Current	A
J	Current density	$A \cdot m^{-2}$
j_{Far}	Microscopic faradaic current density	$A \cdot m^{-2}$
k	Kinetic rate	$mol^{0.5} \cdot m^{-0.5} \cdot s^{-1}$
L_{cat}	Cathode thickness	m
L_{sep}	Separator thickness	m
n	Amount of substance	mol
$M_{Li_2O_2}$	Li_2O_2 Molar mass	$g \cdot mol^{-1}$
P	Number of bins in the separator	-
Q	Number of bins in the cathode	-
R	Universal gas constant	$J \cdot mol^{-1} \cdot K^{-1}$
R_S	Series resistance	$\Omega \cdot m^2$
R_{film}	Thin film resistivity	$\Omega \cdot m$
r	Pore radius	nm
r_{max}	Maximum pore size considered	nm
s	Saturation	–
t	Time	s
T	Temperature	K
U	Cell voltage	V
U_0	Open circuit potential of the cathode	V
V	Volume	m^3
x	1-D spatial coordinate	m
α	Surface area distribution function	nm^{-1}
α_0	Initial surface area distribution function	nm^{-1}
β	Charge transfer coefficient	-
δ	Thickness of discharge product	nm
Δx	Width of a bin	m
ε	Porosity	-
ε_0	Initial porosity	-
ε_{cat}	Cathode porosity	-
ε_{sep}	Separator porosity	-
η	Butler-Volmer overpotential	V
λ	Escape function for O_2^- dissolution	–
ν	Electrons involved in a reaction	-
ξ	Escape probability factor	-
$\rho_{Li_2O_2}$	Li_2O_2 density	$g \cdot m^{-3}$
ϱ	Resistivity of (defective) Li_2O_2	$\Omega \cdot m$
χ	Escape function for O_2^- diffusion	–

References

1. K. M. Abraham and Z. Jiang, *J. Electrochem. Soc.*, **143**, 1 (1996).
2. P. G. Bruce, S. A. Freunberger, L. J. Hardwick, and J.-M. Tarascon, *Nat. Mater.*, **11**, 19 (2012).
3. J. Xiao, D. Mei, X. Li, W. Xu, D. Wang, G. L. Graff, W. D. Bennett, Z. Nie, L. V. Saraf, I. A. Aksay, J. Liu, and J.-G. Zhang, *Nano Lett.*, **11**, 5071 (2011).
4. Z. Peng, S. A. Freunberger, Y. Chen, and P. G. Bruce, *Science*, **337**, 563 (2012).
5. H.-G. Jung, J. Hassoun, J.-B. Park, Y.-K. Sun, and B. Scrosati, *Nat. Chem.*, **4**, 579 (2012).
6. S. S. Zhang, D. Foster, and J. Read, *J. Power Sources*, **195**, 1235 (2010).
7. G. Girishkumar, B. McCloskey, A. C. Luntz, S. Swanson, and W. Wilcke, *J. Phys. Chem. Lett.*, **1**, 2193 (2010).
8. J. Christensen, P. Albertus, R. S. Sanchez-Carrera, T. Lohmann, B. Kozinsky, R. Liedtke, J. Ahmed, and A. Kojic, *J. Electrochem. Soc.*, **159**, R1 (2011).
9. Y.-C. Lu, B. M. Gallant, D. G. Kwabi, J. R. Harding, R. R. Mitchell, M. S. Whittingham, and Y. Shao-Horn, *Energy Environ. Sci.*, **6**, 750 (2013).
10. L.-L. Zhang, Z.-L. Wang, D. Xu, X.-B. Zhang, and L.-M. Wang, *Int. J. Smart Nano Mater.*, **4**, 27 (2013).
11. A. A. Franco and K.-H. Xue, *ECS J. Solid State Sci. Technol.*, **2**, M3084 (2013).
12. M. A. Rahman, X. Wang, and C. Wen, *J. Appl. Electrochem.*, **44**, 5 (2014).
13. S. S. Sandhu, J. P. Fellner, and G. W. Brutchen, *J. Power Sources*, **164**, 365 (2007).
14. P. Andrei, J. P. Zheng, M. Hendrickson, and E. J. Plichta, *J. Electrochem. Soc.*, **157**, A1287 (2010).
15. P. Albertus, G. Girishkumar, B. McCloskey, R. S. Sánchez-Carrera, B. Kozinsky, J. Christensen, and A. C. Luntz, *J. Electrochem. Soc.*, **158**, A343 (2011).
16. Y. Wang, *Electrochimica Acta*, **75**, 239 (2012).
17. X. Li and A. Faghri, *J. Electrochem. Soc.*, **159**, A1747 (2012).
18. J. P. Neidhardt, D. N. Fronczek, T. Jahnke, T. Danner, B. Horstmann, and W. G. Bessler, *J. Electrochem. Soc.*, **159**, A1528 (2012).
19. V. Y. Nimon, S. J. Visco, L. C. D. Jonghe, Y. M. Volfkovich, and D. A. Bograchev, *ECS Electrochem. Lett.*, **2**, A33 (2013).
20. X. J. Chen, V. V. Bevara, P. Andrei, M. Hendrickson, E. J. Plichta, and J. P. Zheng, *J. Electrochem. Soc.*, **161**, A1877 (2014).
21. L. Johnson, C. Li, Z. Liu, Y. Chen, S. A. Freunberger, and P. G. Bruce, *ECS Meet. Abstr.*, **MA2014-02**, 52 (2014).
22. L. Johnson, C. Li, Z. Liu, Y. Chen, S. A. Freunberger, J.-M. Tarascon, P. C. Ashok, B. B. Praveen, K. Dholakia, and P. G. Bruce, *Nat. Chem.*, **6**, 1091 (2014).
23. R. R. Mitchell, B. M. Gallant, Y. Shao-Horn, and C. V. Thompson, *J. Phys. Chem. Lett.*, **4**, 1060 (2013).
24. B. D. Adams, C. Radtke, R. Black, M. L. Trudeau, K. Zaghib, and L. F. Nazar, *Energy Environ. Sci.*, **6**, 1772 (2013).
25. V. Viswanathan, K. S. Thygesen, J. S. Hummelshøj, J. K. Nørskov, G. Girishkumar, B. D. McCloskey, and A. C. Luntz, *J. Chem. Phys.*, **135**, 214704 (2011).
26. M. D. Radin and D. J. Siegel, *Energy Environ. Sci.*, **6**, 2370 (2013).
27. C. O. Laoire, S. Mukerjee, K. M. Abraham, E. J. Plichta, and M. A. Hendrickson, *J. Phys. Chem. C*, **113**, 20127 (2009).
28. C. O. Laoire, S. Mukerjee, K. M. Abraham, E. J. Plichta, and M. A. Hendrickson, *J. Phys. Chem. C*, **114**, 9178 (2010).
29. B. M. Gallant, D. G. Kwabi, R. R. Mitchell, J. Zhou, C. V. Thompson, and Y. Shao-Horn, *Energy Environ. Sci.*, **6**, 2518 (2013).
30. B. Horstmann, B. Gallant, R. Mitchell, W. G. Bessler, Y. Shao-Horn, and M. Z. Bazant, *J. Phys. Chem. Lett.*, **4**, 4217 (2013).
31. M. Safari, B. D. Adams, and L. F. Nazar, *J. Phys. Chem. Lett.*, **5**, 3486 (2014).
32. V. Bevara and P. Andrei, *J. Electrochem. Soc.*, **161**, A2068 (2014).
33. C. Y. Jung, T. S. Zhao, and L. An, *J. Power Sources*, **273**, 440 (2015).
34. K.-H. Xue, T.-K. Nguyen, and A. A. Franco, *J. Electrochem. Soc.*, **161**, E3028 (2014).
35. A. A. Franco, *RSC Adv.*, **3**, 13027 (2013).
36. M. M. Ottakam Thotiyl, S. A. Freunberger, Z. Peng, Y. Chen, Z. Liu, and P. G. Bruce, *Nat. Mater.*, **12**, 1050 (2013).
37. J. Xiao, D. Wang, W. Xu, D. Wang, R. E. Williford, J. Liu, and J.-G. Zhang, *J. Electrochem. Soc.*, **157**, A487 (2010).
38. M. Olivares-Marín, P. Palomino, E. Enciso, and D. Tonti, *J. Phys. Chem. C*, **118**, 20772 (2014).
39. Y.-C. Lu, D. G. Kwabi, K. P. C. Yao, J. R. Harding, J. Zhou, L. Zuin, and Y. Shao-Horn, *Energy Environ. Sci.*, **4**, 2999 (2011).
40. D. Zhai, H.-H. Wang, J. Yang, K. C. Lau, K. Li, K. Amine, and L. A. Curtiss, *J. Am. Chem. Soc.*, **135**, 15364 (2013).
41. V. Viswanathan, J. K. Nørskov, A. Speidel, R. Scheffler, S. Gowda, and A. C. Luntz, *J. Phys. Chem. Lett.*, **4**, 556 (2013).
42. M. A. Quiroga, K.-H. Xue, T.-K. Nguyen, M. Tułodziecki, H. Huang, and A. A. Franco, *J. Electrochem. Soc.*, **161**, E3302 (2014).
43. J. S. Hummelshøj, J. Blomqvist, S. Datta, T. Vegge, J. Rossmeisl, K. S. Thygesen, A. C. Luntz, K. W. Jacobsen, and J. K. Nørskov, *J. Chem. Phys.*, **132**, 071101 (2010).
44. J. M. Garcia-Lastra, J. D. Bass, and K. S. Thygesen, *J. Chem. Phys.*, **135**, 121101 (2011).
45. M. D. Radin, F. Tian, and D. J. Siegel, *J. Mater. Sci.*, **47**, 7564 (2012).
46. O. Gerbig, R. Merkle, and J. Maier, *Adv. Mater.*, **25**, 3129 (2013).
47. S. P. Ong, Y. Mo, and G. Ceder, *Phys. Rev. B*, **85**, 081105 (2012).
48. I. Kowalczk, J. Read, and M. Salomon, *Pure Appl. Chem.*, **79**, 851 (2007).
49. S. H. Oh, T. Yim, P. Ekaterina, and L. F. Nazar, *Electrochem. Solid-State Lett.*, **14**, A185 (2011).
50. Z. H. Cui, X. X. Guo, and H. Li, *Energy Environ. Sci.* (2015).
51. D. Brouillette, G. Perron, and J. E. Desnoyers, *J. Solut. Chem.*, **27**, 151 (1998).
52. A. Pal and Y. P. Singh, *J. Chem. Eng. Data*, **41**, 1008 (1996).
53. V. Gutmann, *Electrochimica Acta*, **21**, 661 (1976).
54. R. G. LeBel and D. A. I. Goring, *J. Chem. Eng. Data*, **7**, 100 (1962).
55. J. Read, K. Mutolo, M. Ervin, W. Behl, J. Wolfenstine, A. Driedger, and D. Foster, *J. Electrochem. Soc.*, **150**, A1351 (2003).
56. http://www.modeling-electrochemistry.com.
57. S. Meini, M. Piana, H. Beyer, J. Schwämmlein, and H. A. Gasteiger, *J. Electrochem. Soc.*, **159**, A2135 (2012).